

Interfacial friction between semiflexible polymers and crystalline surfaces

Nikolai V. Priezjev

Department of Mechanical Engineering, Michigan State University, East Lansing, Michigan 48824, USA

(Received 16 February 2012; accepted 24 May 2012; published online 11 June 2012)

The results obtained from molecular dynamics simulations of the friction at an interface between polymer melts and weakly attractive crystalline surfaces are reported. We consider a coarse-grained bead-spring model of linear chains with adjustable intrinsic stiffness. The structure and relaxation dynamics of polymer chains near interfaces are quantified by the radius of gyration and decay of the time autocorrelation function of the first normal mode. We found that the friction coefficient at small slip velocities exhibits a distinct maximum which appears due to shear-induced alignment of semiflexible chain segments in contact with solid walls. At large slip velocities, the friction coefficient is independent of the chain stiffness. The data for the friction coefficient and shear viscosity are used to elucidate main trends in the nonlinear shear rate dependence of the slip length. The influence of chain stiffness on the relationship between the friction coefficient and the structure factor in the first fluid layer is discussed. © 2012 American Institute of Physics. [<http://dx.doi.org/10.1063/1.4728106>]

I. INTRODUCTION

Understanding the interfacial rheology of complex fluids is important in many processes relevant to technological applications including polymer processing,^{1,2} boundary lubrication,³ and dewetting of polymer films.⁴ Numerous experimental studies have demonstrated that flow velocity profiles in nanoconfined systems can be significantly influenced by slip at polymer-solid interfaces.^{5,6} The measure of slippage is the so-called slip length, which is defined as the distance between the physical interface and imaginary plane where the extrapolated velocity profile reaches the substrate velocity. During the last two decades, the dependence of the slip length on flow conditions and material properties of substrates was extensively investigated by molecular dynamics (MD) simulations for monatomic^{7–26} and polymeric^{27–45} fluids.

In the case of simple shear flow illustrated schematically in Fig. 1, the shear stress is the same in the bulk of the channel and at the interface; and, therefore, the slip length can be calculated from the ratio of the fluid viscosity to the friction coefficient at the interface according to

$$L_s = \frac{\mu}{k}, \quad (1)$$

where the friction coefficient k is defined by the relation between the slip velocity and wall shear stress.⁴⁶ At equilibrium, both the fluid viscosity^{47,48} and friction coefficient^{12,16,24,49} can be estimated from the Green-Kubo relations, and the slip length in the limit of zero shear rate is then computed from Eq. (1). In the presence of flow, the fluid viscosity and friction coefficient might depend on shear rate and slip velocity respectively; and, as a result, the slip length is often a nonlinear function of shear rate.^{10,14,22–24,36,38,42} For example, it was recently shown that at an interface between unentangled polymer melts and passive surfaces (no chemical bonds with the surface and weak wall-fluid interaction energy), the slip length passes through a local minimum at low shear rates and

then increases rapidly at higher shear rates.^{36,42} This non-monotonic behavior was explained by computing the rate-dependent viscosity and the friction coefficient that undergoes a transition from a constant value to the power-law decay as a function of the slip velocity.^{36,42} One of the motivations of the present study is to examine whether these conclusions hold for different simulation ensembles and intramolecular potentials.

In the past two decades, a number of MD studies have demonstrated that the degree of slip at the interface between molecular liquids and crystalline surfaces depends on the structure of the first fluid layer in contact with the periodic surface potential.^{9,12–16,36,39,42} In general, the interfacial slip is suppressed with increasing height of the peak in the fluid structure factor computed at the main reciprocal lattice vector. In turn, the in-plane order within the adjacent fluid layer is determined by several factors, including the commensurability of the liquid and solid structures,^{9,12–14,42} wall-fluid interaction energy,^{9,12,14,18,42} surface rigidity,^{9,15,19,42} molecular structure,^{16,28,35,42,43} and fluid pressure.^{11,28,39,42} Interestingly, recent simulation results have shown that the friction coefficient in the linear slip regime is a function of a combined variable that is a product of the height of the main peak in the structure factor and the contact density of the first fluid layer near the solid wall.⁴² However, at present, there exists no exact relationship between the friction coefficient (or the slip length) and the microscopic properties of the liquid-solid interface.

The formation of the interfacial fluid layer and hydrodynamic boundary conditions can be significantly affected by the polymer chain architecture. For instance, several MD studies have reported flow profiles with a finite slip velocity in thin alkane films where stiff polymer chains tend to align in layers parallel to the surface.^{27,31–33} On the other hand, a weaker density layering near the wall and pronounced slippage were observed for branched alkane molecules.³⁴ Notably, it was demonstrated that upon increasing the length of linear, freely-jointed chains, the structure of the first fluid

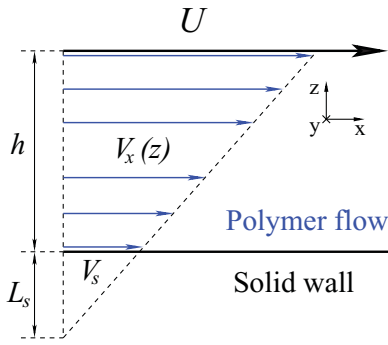


FIG. 1. A schematic view of the Couette flow configuration with slip at the lower and upper walls. Steady shear flow is generated by the upper wall moving with a constant velocity U in the \hat{x} direction while the lower wall is at rest. The slip length and the slip velocity are related via $V_s = \dot{\gamma} L_s$, where $\dot{\gamma}$ is the shear rate computed from the slope of the velocity profile.

layer near a solid wall is reduced, resulting in smaller values of the friction coefficient and larger slip lengths at low shear rates.³⁵ Later, it was found that the existence and location of a double bond along the backbone of linear oligomers affect the structure of the interfacial fluid layer near crystalline aluminum walls and lead to either negative or large positive slip lengths.⁴¹ More recently, it was shown that slip velocity is reduced for liquids which consist of molecules that can easily conform their atoms into low-energy sites of the substrate potential.⁴³ Despite extensive research on the fluid structure and shear response in thin polymer films, it is often difficult to predict even qualitatively the influence of liquid molecular structure on the interfacial slip.

In this paper, we investigate the effect of chain bending stiffness on the fluid structure and friction coefficient at interfaces between linear polymers and crystalline surfaces. We will show that the relaxation dynamics near weakly attractive surfaces is significantly slowed down for stiffer chains at equilibrium. The orientation of semiflexible chains in shear flow leads to the enhanced density layering away from the walls and partial alignment of extended chain segments in the first fluid layer. It will be demonstrated that the shear-induced ordering of the chain segments produces a distinct maximum in the liquid structure factor and the friction coefficient at small slip velocities. Finally, the characteristic features in the shear rate dependence of the slip length are interpreted in terms of the shear-thinning viscosity and the dynamic friction coefficient.

The rest of this paper is organized as follows. The details of molecular dynamics simulations, interaction potentials, and equilibration procedure are described in Sec. II. The simulation results are presented in Sec. III. More specifically, the chain conformation and relaxation dynamics are analyzed in Subsection III A, examples of density and velocity profiles are presented in Subsection III B, shear viscosity and slip lengths are reported in Subsection III C, the velocity dependence of the friction coefficient is examined in Subsection III D, and, finally, the fluid structure near solid walls is considered in Subsection III E. Brief conclusions are given in the last section.

II. MOLECULAR DYNAMICS SIMULATION MODEL

We consider a coarse-grained bead-spring model of unentangled polymer melt, which consists of $M = 480$ linear chains of $N = 20$ beads (or monomers) each. In this model any two fluid monomers interact via the truncated Lennard-Jones (LJ) potential

$$V_{LJ}(r) = 4\varepsilon \left[\left(\frac{\sigma}{r} \right)^{12} - \left(\frac{\sigma}{r} \right)^6 \right], \quad (2)$$

where ε and σ are the energy and length scales of the fluid phase. The cutoff radius $r_c = 2.5\sigma$ and the total number of fluid monomers $N_f = 9600$ are fixed throughout all simulations. Similarly, fluid monomers interact with wall atoms via the LJ potential with the following parameters $\varepsilon_{wf} = 0.8\varepsilon$, $\sigma_{wf} = \sigma$, and $r_c = 2.5\sigma$.

Any two consecutive beads in a polymer chain interact through the finitely extensible nonlinear elastic (FENE) potential⁵⁰

$$V_{FENE}(r) = -\frac{k_s}{2} r_o^2 \ln [1 - r^2/r_o^2], \quad (3)$$

with the standard parameters $k_s = 30\varepsilon\sigma^{-2}$ and $r_o = 1.5\sigma$.⁵¹ The combination of LJ and FENE potentials yields an effective bond potential between the nearest-neighbor beads with the average bond length $b = 0.97\sigma$.⁵¹ This bond potential is strong enough to prevent chain crossing and breaking even at the highest shear rates considered in the present study. In addition, the flexibility of polymer chains is controlled by the bending potential as follows:

$$U_{bend}(\theta) = k_\theta (1 - \cos \theta), \quad (4)$$

where k_θ is the bending stiffness coefficient and θ is the angle between two consecutive bonds along a polymer chain.⁵² In the present study, the bending stiffness coefficient was varied in the range $0 \leq k_\theta \leq 3.5\varepsilon$. A snapshot of the confined polymer melt that consists of semiflexible linear chains with the bending coefficient $k_\theta = 2.5\varepsilon$ is shown in Figure 2.

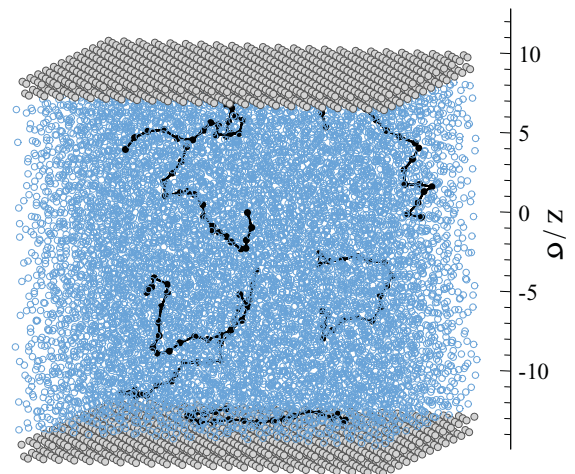


FIG. 2. Instantaneous positions of fluid monomers (open blue circles) and fcc wall atoms (filled gray circles) at equilibrium (i.e., both walls are at rest). Each monomer belongs to a polymer chain ($N = 20$) with the bending stiffness coefficient $k_\theta = 2.5\varepsilon$. Seven chains are indicated by thick solid lines and filled black circles. The fluid monomer density is $\rho = 0.91\sigma^{-3}$ and the wall atom density is $\rho_w = 1.40\sigma^{-3}$.

In order to remove viscous heating generated in the shear flow, the motion of fluid monomers was coupled to an external heat bath via a Langevin thermostat⁵³ applied in the \hat{y} direction to avoid bias in the shear flow direction (the \hat{x} direction). This is a standard thermostating procedure often used in MD simulations of sheared fluids.^{9,10,28,54,55} Thus, the equations of motion for fluid monomers are summarized as follows:

$$m\ddot{x}_i = - \sum_{i \neq j} \frac{\partial V_{ij}}{\partial x_i}, \quad (5)$$

$$m\ddot{y}_i + m\Gamma\dot{y}_i = - \sum_{i \neq j} \frac{\partial V_{ij}}{\partial y_i} + f_i, \quad (6)$$

$$m\ddot{z}_i = - \sum_{i \neq j} \frac{\partial V_{ij}}{\partial z_i}, \quad (7)$$

where $\Gamma = 1.0 \tau^{-1}$ is the friction coefficient that controls the damping term, V_{ij} is the total interaction potential, and f_i is a random force with zero mean and variance $\langle f_i(0)f_j(t) \rangle = 2mk_B T \delta(t)\delta_{ij}$ obtained from the fluctuation-dissipation theorem. The Langevin thermostat temperature is set $T = 1.1\varepsilon/k_B$, where k_B refers to the Boltzmann constant. The equations of motion were solved numerically using the fifth-order Gear predictor-corrector algorithm⁵⁶ with a time step $\Delta t = 0.005 \tau$, where $\tau = \sqrt{m\sigma^2/\varepsilon}$ is the LJ time. Typical values of the length, energy, and time scales for hydrocarbon chains are $\sigma = 0.5 \text{ nm}$, $\varepsilon = 30 \text{ meV}$, and $\tau = 3 \times 10^{-12} \text{ s}$.⁵⁶

The polymer melt is confined between two crystalline walls as illustrated in Figure 2. Each wall consists of 1152 atoms distributed between two layers of the face-centered cubic (fcc) lattice with density $\rho_w = 1.40\sigma^{-3}$. For computational efficiency, the wall atoms are fixed rigidly to the wall lattice sites, which form two (111) planes with $[11\bar{2}]$ orientation parallel to the \hat{x} direction. The nearest-neighbor distance between the lattice sites within the (111) plane is $d = 1.0\sigma$ and the first reciprocal lattice vector in the \hat{x} direction is $\mathbf{G}_1 = (7.23\sigma^{-1}, 0)$. The channel dimensions in the xy plane are measured to be $L_x = 20.86\sigma$ and $L_y = 24.08\sigma$. Periodic boundary conditions were applied along the \hat{x} and \hat{y} directions parallel to the solid walls.

In our simulations, the distance between the wall lattice planes, which are in contact with the fluid phase, was fixed at $h = 22.02\sigma$. Hence, the volume accessible to the fluid phase corresponds to the fluid monomer density $\rho = N_f/L_x L_y (h - \sigma) = 0.91\sigma^{-3}$; and, in the absence of shear flow, the resulting fluid pressure and temperature are $1.0\varepsilon\sigma^{-3}$ and $1.1\varepsilon/k_B$, respectively. In the present study, the relatively low polymer density (or normal pressure) was chosen based on the results from our previous study where it was shown that for weak wall-fluid interactions and $\rho \leq 1.02\sigma^{-3}$ (or $P \leq 5.0\varepsilon\sigma^{-3}$), the fluid velocity profiles remain linear in a wide range of shear rates.³⁶ In contrast, it was demonstrated that at higher polymer densities (or pressures), the velocity profiles acquire a pronounced curvature near the wall and the relaxation of flexible polymer chains in the interfacial region becomes very slow.³⁹

The system was first equilibrated for about $5 \times 10^4 \tau$ while both walls were at rest. Then, the velocity of the upper

wall was increased gradually up to a target value, followed by an additional equilibration period of about $5 \times 10^4 \tau$. In this study, the upper wall velocity was varied over about three orders of magnitude $0.005 \leq U\tau/\sigma \leq 5.5$. Once the steady shear flow was generated, the velocity, density, and temperature profiles were averaged within horizontal bins of thickness $\Delta z = 0.01\sigma$ for a time period up to $5 \times 10^5 \tau$. At the lowest upper wall speed, $U = 0.005\sigma/\tau$, the velocity profiles were computed in 24 independent systems for the total time period of about $5 \times 10^6 \tau$. An upper estimate of the Reynolds number at high shear rates is $Re = \rho h U / \mu = O(10)$, which is indicative of laminar flow conditions in the channel.

We finally note that MD simulations were also performed at a constant normal load, where the distance between the walls was allowed to vary under the constant normal pressure $P_\perp = 1.0\varepsilon\sigma^{-3}$ applied to the upper wall. However, we did not observe any qualitatively new behavior; and for the sake of brevity, these results are not reported in the present study.

III. RESULTS

A. Chain conformation and relaxation dynamics

The spatial configuration of polymer chains is well characterized by the radius of gyration, which is defined as the average distance between monomers in a polymer chain and its center of mass as follows:

$$R_g^2 = \frac{1}{N} \sum_{i=1}^N (\mathbf{r}_i - \mathbf{r}_{\text{cm}})^2, \quad (8)$$

where \mathbf{r}_i is the position vector of the i th monomer, $N = 20$ is the number of monomers per chain, and \mathbf{r}_{cm} is the chain center of mass defined as

$$\mathbf{r}_{\text{cm}} = \frac{1}{N} \sum_{i=1}^N \mathbf{r}_i. \quad (9)$$

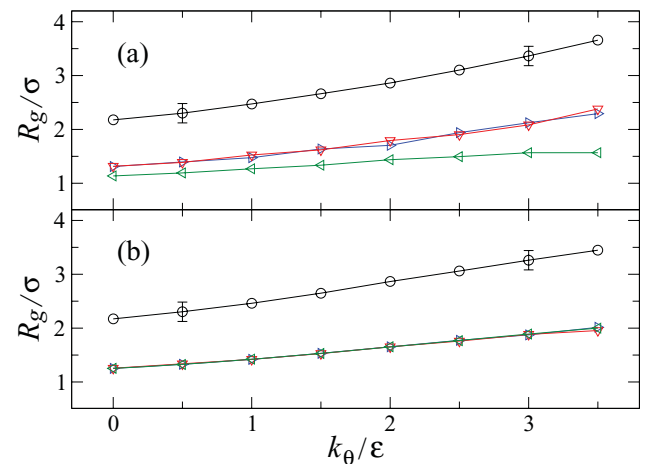


FIG. 3. The ensemble averaged \hat{x} , \hat{y} , and \hat{z} components of the radius of gyration R_{gx} (\blacktriangleright), R_{gy} (∇), R_{gz} (\triangleleft), and the total radius of gyration R_g (\circ) as a function of k_θ for polymer chains (a) in contact with the solid walls and (b) in the bulk region. The simulations were performed at the constant fluid density $\rho = 0.91\sigma^{-3}$ while both walls were at rest.

Figure 3 shows the radius of gyration and its components along the \hat{x} , \hat{y} , and \hat{z} directions as a function of the bending stiffness coefficient. The chain statistics were collected in the interfacial regions (where at least one monomer in a chain is in contact with wall atoms) and in the middle of the channel (the chain center of mass is located further than 6σ away from the walls). As expected, in both cases R_g increases with increasing chain stiffness. Note that even at the largest value of the bending stiffness coefficient $k_\theta = 3.5\epsilon$, the size of polymer chains is smaller than the channel dimensions. The simulation results in Fig. 3 indicate that in the bulk region the chain configuration is isotropic, while near the interfaces polymer chains become flattened, i.e., $R_{gz} < R_{gx} \approx R_{gy}$, which is in agreement with previous MD studies.^{57–59} It is also apparent that fully flexible chains in contact with the walls are packed on average within the first two fluid layers [$2R_{gz} \approx 2\sigma$ for $k_\theta = 0$ in Fig. 3(a)]. In contrast, semiflexible chains extend up to about three molecular diameters from the walls. Visual inspection of the polymer chains in the interfacial regions revealed that the conformation of semiflexible chains consists of locally extended segments within the first fluid layer and segments of several monomers oriented away from the walls. Finally, regardless of the chain stiffness, the total radius of gyration is nearly the same in the bulk and close to the walls due to the relatively weak wall-fluid interaction energy.

The local relaxation dynamics in confined polymer films can be described by the decay of the time autocorrelation function of normal modes.^{39,58,60,61} By definition, the normal coordinates for a free polymer chain that consists of N monomers are given by

$$\mathbf{X}_p(t) = \frac{1}{N} \sum_{i=1}^N \mathbf{r}_i(t) \cos \frac{p\pi(i-1)}{N-1}, \quad (10)$$

where \mathbf{r}_i is the position vector of the i th monomer in the chain, and $p = 0, 1, \dots, N-1$ is the mode number.^{51,58,62} The longest relaxation time corresponds to the first mode $p = 1$, i.e., to the relaxation of the whole chain.⁶² The normalized time autocorrelation function for the first normal mode is then defined as follows:

$$C_1(t) = \langle \mathbf{X}_1(t) \cdot \mathbf{X}_1(0) \rangle / \langle \mathbf{X}_1(0) \cdot \mathbf{X}_1(0) \rangle. \quad (11)$$

In our study, the autocorrelation function [Eq. (11)] was computed separately in the interfacial regions (where the chain center of mass is confined within 3σ from the walls) and in the bulk of the channel where the fluid density is uniform (the center of mass is located at least 6σ away from the walls). An important aspect is that the autocorrelation function was averaged only for those polymer chains whose centers of mass remained within either the interfacial or bulk regions during the relaxation time interval.

Figure 4 shows the relaxation of the time autocorrelation function at equilibrium (i.e., when both walls are at rest) for selected values of the bending stiffness coefficient. As is evident from Fig. 4(a), the relaxation rate of polymer chains in the bulk region decreases with increasing bending stiffness. A similar effect was reported previously for linear bead-spring chains with variable bending rigidity,⁶³ indicating that the re-orientation dynamics in the melt is slowed down for more

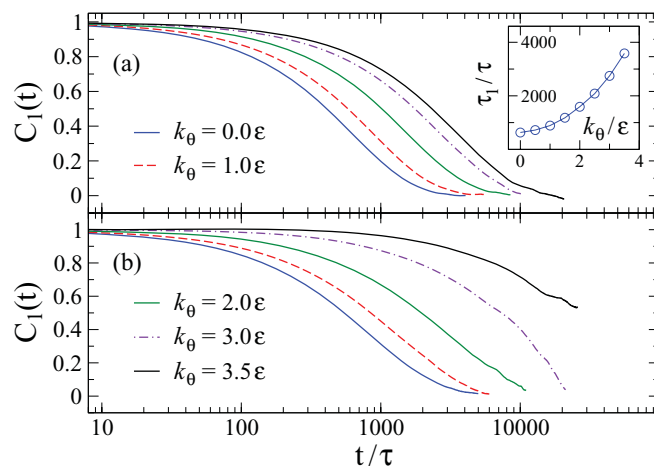


FIG. 4. The time autocorrelation function of the first normal mode Eq. (11) for polymer chains (a) in the bulk region and (b) near the walls for several values of the bending stiffness coefficient. The inset shows the relaxation time of polymer chains in the bulk.

rigid polymer chains. In our study, the decay rate of the autocorrelation function in the bulk is well described by the exponential function $C_1(t) = \exp(-t/\tau_1)$, where τ_1 is the characteristic relaxation time. The inset in Fig. 4(a) presents the variation of τ_1 as a function of the bending stiffness coefficient. The inverse relaxation time, $1/\tau_1$, is related to the characteristic shear rate, above which the shear viscosity is expected to exhibit non-Newtonian behavior (see discussion below). We note that for stiffer chains, the estimated shear rate is about $2.5 \times 10^{-4} \tau^{-1}$, which is about the lowest shear rate accessible in coarse-grained MD simulations (without excessive computational time requirements).

In contrast, the decay in time of the autocorrelation function is much slower for semiflexible polymer chains in the interfacial regions, see Fig. 4(b). Similar results were observed previously in MD simulations of freely-jointed 5-mers adsorbed on weakly physisorbing surfaces, i.e., the relaxation time of adsorbed chains is about an order of magnitude larger than in the bulk.⁶⁰ In our setup, the relaxation time of flexible chains in the interfacial region is only slightly larger than in the bulk, which means that the relaxation dynamics is weakly affected by the substrate. With increasing chain stiffness, however, the rotational relaxation is significantly slowed down. The data shown in Fig. 4(b) cannot be well fitted by the single exponential function. We comment that the typical relaxation time for polymer chains in the interfacial regions was used to determine the time interval for averaging the radius of gyration and bond orientation. It should also be mentioned that test simulations of polymer chains with larger stiffness coefficients, $k_\theta = 4.0\epsilon$ and 4.5ϵ , have shown that their relaxation dynamics near interfaces is extremely slow and cannot be accurately resolved (results not reported).

B. Fluid density, velocity, and temperature profiles

The averaged monomer density profiles are presented in Fig. 5 for fully flexible ($k_\theta = 0.0\epsilon$) and semiflexible ($k_\theta = 3.0\epsilon$) polymer chains at small ($U = 0.01\sigma/\tau$) and large

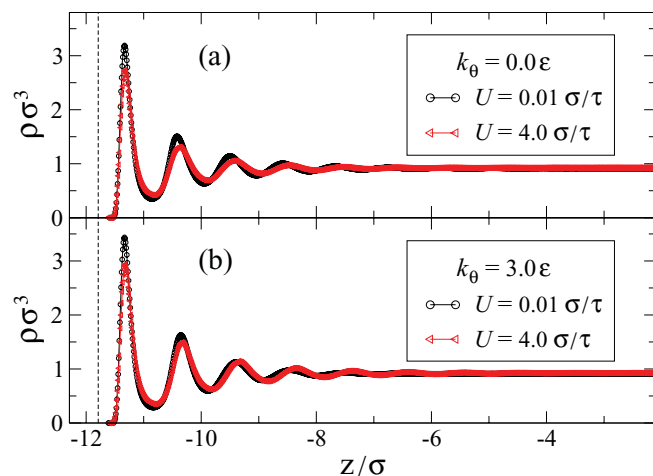


FIG. 5. Averaged monomer density profiles near the lower stationary wall for the indicated values of the upper wall velocity U and $\rho = 0.91\sigma^{-3}$. The bending stiffness coefficients are (a) $k_\theta = 0.0\epsilon$ and (b) $k_\theta = 3.0\epsilon$. The left vertical axis at $z = -12.29\sigma$ coincides with the fcc lattice plane in contact with the polymer melt. The vertical dashed line at $z = -11.79\sigma$ denotes the location of the liquid-solid interface.

($U = 4.0\sigma/\tau$) upper wall velocities. Near the solid walls, these profiles exhibit typical density oscillations that gradually decay to a uniform profile in the middle of the channel. Notice that the magnitude of the first peak in the density profiles (defined as the contact density) is higher for stiffer polymer chains. For example, the contact density is $\rho_c = 3.19\sigma^{-3}$ for flexible chains and $\rho_c = 3.44\sigma^{-3}$ for $k_\theta = 3.0\epsilon$ when the upper wall velocity is $U = 0.01\sigma/\tau$ in Fig. 5. This result, at first glance, appears to be somewhat counterintuitive because one might expect that flexible chains can pack more effectively near a flat surface. However, with increasing bending rigidity, the persistence length of polymer chains increases; and, therefore, the first fluid layer contains more extended chain segments. When $U = 0.01\sigma/\tau$ in Fig. 5, the average number of consecutive monomers per polymer chain in the first fluid layer is $N_{seg} \approx 3.1$ for flexible chains and $N_{seg} \approx 5.2$ for $k_\theta = 3.0\epsilon$. It turns out that these locally extended chain segments arrange themselves more tightly near the surface. We also note that similar trends in the fluid density layering were reported in other coarse-grained MD simulations; namely, that with increasing length of (semi)flexible polymer chains, the amplitude of density oscillations near a solid wall becomes (larger) smaller.^{32,57}

As shown in Fig. 5(a), the height of the density peaks in the case of flexible chains is reduced at the higher upper wall speed $U = 4.0\sigma/\tau$. At these flow conditions, the slip velocity of the first fluid layer is relatively large (of about $1.0\sigma/\tau$), and the temperature of the fluid near the walls is higher than the temperature of the Langevin thermostat, leading to a reduced density layering. This is consistent with the results of previous MD studies where the shear response of thin polymer films was examined in a wide range of shear rates.^{36,39,42} Interestingly, while the amplitude of the first two peaks in the density profile for semiflexible chains ($k_\theta = 3.0\epsilon$) is also reduced at the higher upper wall speed $U = 4.0\sigma/\tau$, the orientation of more rigid chain segments along the shear flow

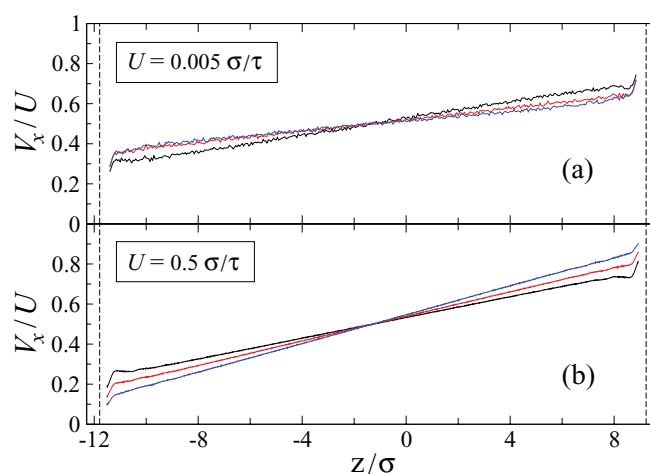


FIG. 6. Averaged normalized velocity profiles for the upper wall speeds (a) $U = 0.005\sigma/\tau$ and (b) $U = 0.5\sigma/\tau$ and bending stiffness coefficients $k_\theta = 0.0\epsilon$ (black lines), $k_\theta = 2.0\epsilon$ (red lines), and $k_\theta = 3.0\epsilon$ (blue lines). The vertical axes coincide with the location of the fcc lattice planes (at $z/\sigma = -12.29$ and 9.73). The vertical dashed lines (at $z/\sigma = -11.79$ and 9.23) indicate reference planes for computing the slip length.

direction produces slightly higher density in the 3rd, 4th, and 5th fluid layers [see Fig. 5(b)].

The representative velocity profiles are plotted in Fig. 6 for the lowest $U = 0.005\sigma/\tau$ and intermediate $U = 0.5\sigma/\tau$ upper wall speeds and $k_\theta = 0.0\epsilon$, 2.0ϵ , and 3.0ϵ . For $U = 0.005\sigma/\tau$, despite extensive averaging, the data remain noisy because the average flow velocity is much smaller than the thermal fluid velocity $v_T = k_B T/m$. In all cases, the velocity profiles are anti-symmetric with respect to the center of the channel and linear except within about 2σ near the walls. Surprisingly, the dependence of slip velocity on bending stiffness shows opposite trends for the reported upper wall speeds; namely, the slip velocity for flexible chains is smaller for $U = 0.005\sigma/\tau$ in Fig. 6(a), while it is larger for $U = 0.5\sigma/\tau$ in Fig. 6(b). This result illustrates that the effect of chain stiffness on the interfacial slip strongly depends on flow conditions. In what follows, the shear rate was extracted from the linear part of velocity profiles excluding the interfacial regions of about 4σ . As usual, the slip length was computed by linear extrapolation of the velocity profiles to the values $V_x = 0$ below the lower wall and $V_x = U$ above the upper wall and then averaged.

Figure 7 shows the ensemble-averaged temperature profiles for selected values of the upper wall speed and $k_\theta = 0.0\epsilon$ and 3.0ϵ . The local fluid temperature inside the averaging bins was computed from the velocity component in the \hat{z} direction (perpendicular to the walls). As observed in Fig. 7, at small values of the upper wall speed, the fluid temperature is uniform throughout the channel and it remains equal to the temperature imposed by the Langevin thermostat. With increasing upper wall velocity, the fluid heats up and the temperature profiles become curved near the interfaces. When $U = 4.0\sigma/\tau$ in Fig. 7, the heating up is more pronounced near the walls because the slip velocity is comparable to the fluid thermal velocity. We note that it was previously shown that at high shear rates, the fluid temperature in

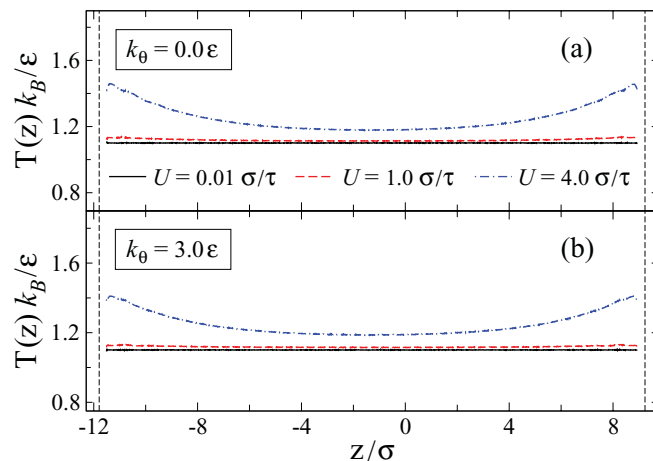


FIG. 7. Temperature profiles across the channel for the indicated values of the upper wall velocity and bending stiffness coefficients (a) $k_\theta = 0.0\varepsilon$ and (b) $k_\theta = 3.0\varepsilon$. The vertical axes denote the location of the fcc lattice planes (at $z/\sigma = -12.29$ and 9.73) in contact with fluid molecules. The dashed lines (at $z/\sigma = -11.79$ and 9.23) mark the position of the liquid-solid interface.

the direction perpendicular to the plane of shear is slightly smaller than in the other directions, indicating that the kinetic energy in the \hat{y} direction, in which the Langevin thermostat is applied, dissipates faster than the energy transfer from the other directions.³⁶ It should also be mentioned that mechanical and dynamical properties of two-dimensional fluids undergoing planar Couette flow can be affected by the thermostating procedure, which is applied either directly on the fluid molecules or only on the vibrating wall atoms.⁶⁴

C. Shear viscosity and slip length

In steady shear flow, the fluid viscosity is defined by the relation $\sigma_{xz} = \mu(\dot{\gamma})\dot{\gamma}$, where $\dot{\gamma}$ denotes the shear rate and σ_{xz} is the shear stress through any plane parallel to the solid walls. In our simulations, the shear stress was computed at the liquid-solid interface by averaging the total force (in the shear flow direction) between the lower wall atoms

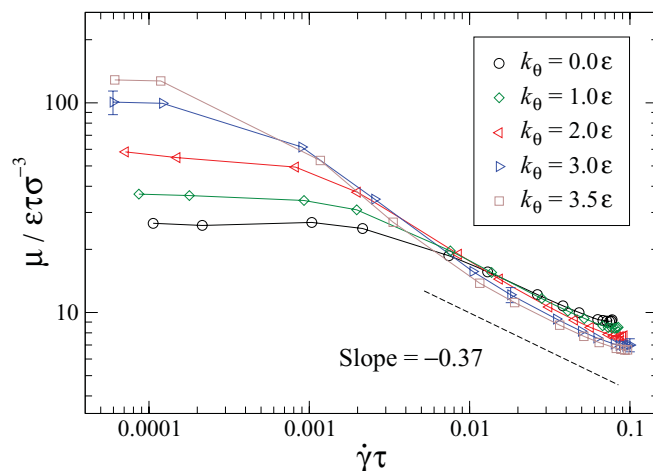


FIG. 8. Shear rate dependence of the polymer viscosity μ (in units of $\varepsilon\tau\sigma^{-3}$) for selected values of the bending stiffness coefficient. The dashed line indicates a slope of -0.37 . Solid curves are a guide for the eye.

and the fluid molecules. The dependence of polymer viscosity on shear rate is presented in Fig. 8 for selected values of the bending stiffness coefficient. For more flexible chains ($k_\theta \leq 2.0\varepsilon$), the gradual transition from the Newtonian to shear-thinning regimes is clearly observed in the accessible range of shear rates. The dashed line with the slope -0.37 is shown for reference in Fig. 8, indicating shear-thinning behavior of flexible chains ($k_\theta = 0.0\varepsilon$ and $N = 20$) reported in previous studies.^{36,42} The characteristic shear rate of the transition correlates well with the inverse relaxation time of polymer chains in the bulk region [see inset in Fig. 4(a)]. Not surprisingly, with increasing chain stiffness, the polymer viscosity at low shear rates increases, and the slope of the shear-thinning region becomes more steep due to the orientation of partially uncoiled chains in the shear flow. The apparent saturation of the viscosity at high shear rates is due to an increase in the fluid temperature near interfaces. The error bars are larger at low shear rates due to the enhanced statistical uncertainty in averaging velocity profiles and wall shear stress.

Figure 9 shows the dependence of slip length as a function of shear rate for the same flow conditions and values of the bending stiffness coefficient as in Fig. 8. All curves in Fig. 9 exhibit the same characteristic features: a pronounced minimum at low shear rates and a steep increase at higher shear rates. In case of flexible chains, this behavior was analyzed previously^{36,39,42} using Eq. (1). As illustrated in Fig. 9, the slip length (for $k_\theta = 0.0\varepsilon$) is nearly constant at low shear rates because of the extended Newtonian regime [in Fig. 8] and velocity-independent friction coefficient. With increasing shear rate, the relative competition between the shear-thinning viscosity and the dynamic friction coefficient in Eq. (1) leads to a minimum in the slip length, which is followed by a rapid increase at higher shear rates. Unexpectedly, increasing the chain stiffness produces larger slip lengths at low shear rates but smaller L_s at high shear rates. This trend can be understood by analyzing the effect of chain stiffness on the friction coefficient as a function of the slip velocity (see Subsection III D).

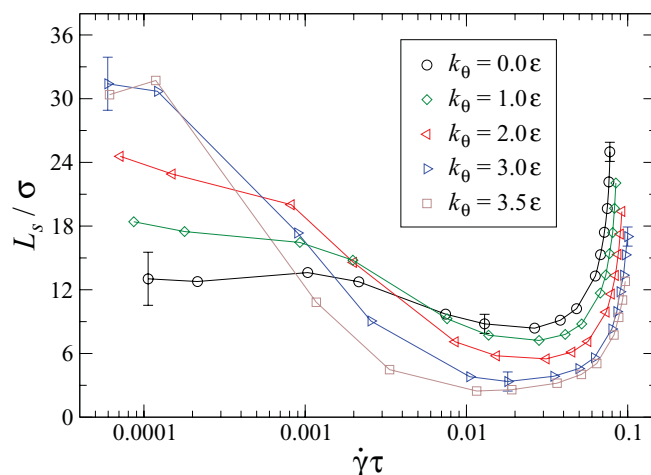


FIG. 9. Variation of the slip length L_s/σ as a function of shear rate for the indicated values of the bending stiffness coefficient. The solid curves are drawn to guide the eye.

As mentioned previously, the range of the upper wall speeds considered in the present study corresponds to anti-symmetric velocity profiles so that the slip velocity is the same at the lower and upper walls. It is expected that at higher upper wall speeds, the slip velocity at one of the solid walls will be much larger than the fluid thermal velocity producing slip lengths much larger than the channel height.³⁸ The investigation of the slip transition at very high shear rates is not the main focus of this paper; and, therefore, it was not studied in detail.

D. The dynamic friction coefficient

In this subsection, we analyze the influence of chain stiffness on the friction coefficient at the liquid-solid interface as a function of the slip velocity. The results of previous MD studies have shown that the data for flexible polymer chains and weakly attractive crystalline surfaces can be well fitted by the following empirical equation:

$$k/k^* = [1 + (V_s/V_s^*)^2]^{-0.35}, \quad (12)$$

where the parameter k^* is the friction coefficient at small slip velocities and V_s^* is the characteristic slip velocity of the transition to the nonlinear regime.^{36,39,42} It was demonstrated numerically that the friction coefficient k^* is determined by the contact density and the in-plane structure factor of the first fluid layer.⁴² Furthermore, the characteristic slip velocity V_s^* was found to correlate well with the diffusion rate of fluid monomers over the distance between nearest minima of the substrate potential.⁴² The physical origin of the exponent -0.35 in Eq. (12) is at present unclear.

Although the friction coefficient can be readily computed from Eq. (1), the slight curvature in the velocity profiles near solid walls and the location of the liquid-solid interfaces used to compute the slip length [see Fig. 6], introduce a small discrepancy between the definitions $k(V_s) = \mu/L_s$ and $k(V_1) = \sigma_{xz}/V_1$, where $V_s = L_s \dot{\gamma}$ and V_1 is the velocity of first fluid layer. To eliminate this uncertainty, in the present study, the slip velocity was computed directly from the velocity profiles as follows:

$$V_1 = \int_{z_0}^{z_1} V_x(z) \rho(z) dz / \int_{z_0}^{z_1} \rho(z) dz, \quad (13)$$

where the limits of integration ($z_0 = -11.54\sigma$ and $z_1 = -10.87\sigma$) define the width of the first peak in density profiles, which are shown for example in Fig. 5.

The friction coefficient $k(V_1)$ as a function of the slip velocity is plotted in Fig. 10 for several values of the bending stiffness coefficient. The important conclusion from the present results is that, with increasing chain stiffness, the friction coefficient at small slip velocities increases, and its decay rate at large slip velocities is independent of the chain stiffness. It can be further observed that for more flexible chains, $k_\theta \leq 1.0\epsilon$, the data are well described by the functional form given by Eq. (12). However, as the chain stiffness increases, the data in Fig. 10 indicate qualitative changes in the velocity dependence of the friction coefficient, i.e., the appearance of a pronounced maximum at small slip velocities. This non-monotonic behavior is related to the enhanced ordering

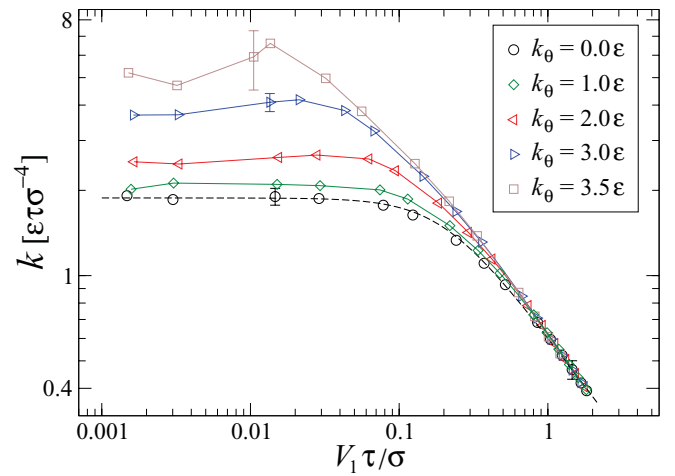


FIG. 10. Log-log plot of the friction coefficient $k = \sigma_{xz}/V_1$ (in units of $\epsilon\tau\sigma^{-4}$) as a function of the slip velocity of the first fluid layer V_1 (in units of σ/τ) for the tabulated values of the bending stiffness coefficient. The dashed curve is the best fit to Eq. (12) with $k^* = 1.88\epsilon\tau\sigma^{-4}$ and $V_s^* = 0.2\sigma/\tau$. The solid curves are guides for the eye.

of semiflexible chains near interfaces due to their orientation along the shear flow direction. This effect will be discussed in more detail in Subsection III E. For the largest value of the stiffness coefficient, $k_\theta = 3.5\epsilon$, the error bars are relatively large at small slip velocities because the orientation of the extended chain segments in the first fluid layer is strongly influenced by the sixfold symmetry of the wall lattice and their relaxation dynamics is very slow [see Fig. 4 (b)].

Nevertheless, some trends in the nonlinear rate dependence of the slip length presented in Fig. 9 can be understood from Eq. (1) and the data reported in Figs. 8 and 10. For example, the ratio of shear viscosity to the friction coefficient is smaller for stiffer chains with $k_\theta = 3.5\epsilon$ at high shear rates, while the largest slip length at low shear rates is reported for chains with $k_\theta = 3.0\epsilon$. Also, the sharp decay of the slip length for the cases $k_\theta = 3.0\epsilon$ and 3.5ϵ in Fig. 9 is related to the large negative slope of the polymer viscosity at low shear rates. As mentioned earlier, the nearly constant value of the slip length at low shear rates for fully flexible chains in Fig. 9 is due to the Newtonian viscosity and a wide linear regime of friction determined by the parameter V_s^* in Eq. (12).

E. Fluid structure near solid walls

The examples of the fluid density profiles shown in Fig. 5 demonstrate that the fluid density layering is most pronounced for the fluid monomers in contact with wall atoms. It is well known that, in addition to the fluid ordering perpendicular to the substrate, the periodic surface potential induces structure formation within the first fluid layer. The measure of the induced order is the in-plane static structure factor, which is defined as follows:

$$S(\mathbf{k}) = \frac{1}{N_\ell} \left| \sum_{j=1}^{N_\ell} e^{i\mathbf{k}\cdot\mathbf{r}_j} \right|^2, \quad (14)$$

where the sum is over N_ℓ fluid monomers in the layer and $\mathbf{r}_j = (x_j, y_j)$ is the position vector of the j th monomer.

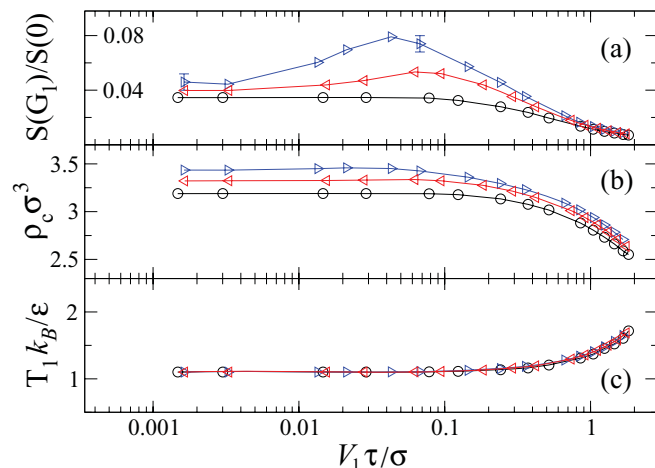


FIG. 11. The normalized structure factor at the main reciprocal lattice vector $\mathbf{G}_1 = (7.23 \sigma^{-1}, 0)$ (a), contact density (b), and temperature (c) of the first fluid layer as a function of the slip velocity V_1 (in units of σ/τ). The values of the bending stiffness coefficient are $k_\theta = 0.0\epsilon$ (\circ), $k_\theta = 2.0\epsilon$ (\triangleleft), and $k_\theta = 3.0\epsilon$ (\triangleright).

Depending on the strength of wall-fluid interactions and commensurability of liquid and solid structures, the structure factor typically contains a set of sharp peaks at the reciprocal lattice vectors, which are superimposed on several concentric rings characteristic of the liquid-like short range order.⁹ In the past, several MD studies have demonstrated a strong correlation between the magnitude of the largest peak at the first reciprocal lattice vector and the friction coefficient at liquid-solid interfaces.^{9,12,14,15,28,35,36,39,42}

We next plot the dependence of the normalized structure factor evaluated at the main reciprocal lattice vector $\mathbf{G}_1 = (7.23 \sigma^{-1}, 0)$, the contact density, and the temperature of the first fluid layer in Fig. 11 for three values of the bending stiffness coefficient. Similar to previous findings for flexible chains,³⁹ all three parameters in Fig. 11 remain constant at small slip velocities, $V_1 \lesssim 0.1 \sigma/\tau$, while the induced structure $[S(\mathbf{G}_1)/S(0)]$ and ρ_c reduces and the fluid temperature increases at higher slip velocities. In sharp contrast, the structure factor for semiflexible chains exhibits a distinctive maximum at small slip velocities. Note that these changes in the structure factor are not reflected in the contact density, suggesting that they are mainly caused by the reorientation of chain segments in the first layer along the shear flow direction.

In order to quantify this hypothesis, we examined the chain structure in contact with the substrate. Figure 12 shows the average number of consecutive monomers per chain in the first fluid layer and their bond orientation with respect to the shear flow direction. Specifically, we computed the average value $\langle \cos^2 \theta \rangle$, where θ is the angle between the \hat{x} axis and the three-dimensional bond vector connecting two consecutive monomers in the first fluid layer. In this definition, $\langle \cos^2 \theta \rangle = 0.5$ for the planar isotropic distribution, whereas $\langle \cos^2 \theta \rangle = 1.0$ for the parallel arrangement of bond vectors along the \hat{x} axis. The plots in Fig. 12 reveal that, with increasing chain stiffness, the first fluid layer consists of more extended chain segments, which become preferentially aligned in the direction of shear flow. Notice that the orientation of

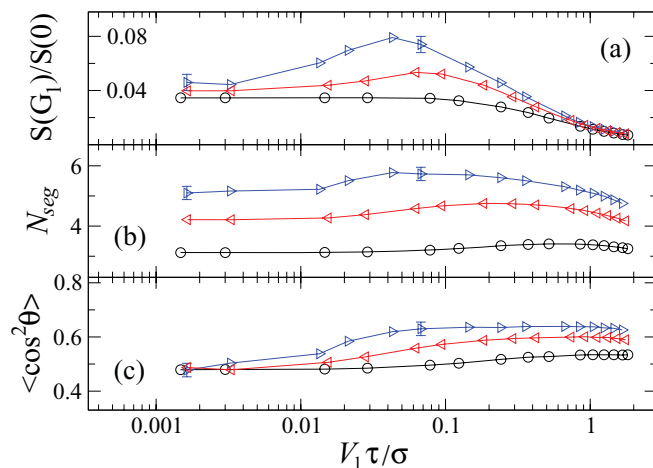


FIG. 12. The structure factor (a), number of consecutive monomers per chain (b), and bond orientation (c) in the first fluid layer as a function of the slip velocity. The values of the bending stiffness coefficient are $k_\theta = 0.0\epsilon$ (\circ), $k_\theta = 2.0\epsilon$ (\triangleleft), and $k_\theta = 3.0\epsilon$ (\triangleright). The data for $S(\mathbf{G}_1)/S(0)$ are the same as in Fig. 11 (a).

flexible chain segments remain isotropic at small slip velocities, $V_1 \lesssim 0.1 \sigma/\tau$. Hence, the results in Figs. 11 and 12 indicate that the appearance of a maximum in $S(\mathbf{G}_1)/S(0)$, which in turn affects the friction coefficient in Fig. 10, is due to the shear-induced alignment of semiflexible chain segments in the first fluid layer.

We finally summarize our data by plotting the inverse friction coefficient as a function of the combined variable $S(0)/[S(\mathbf{G}_1)\rho_c]$ in Fig. 13. It was previously shown for flexible polymer chains that in the linear regime [$V_s < V_s^*$ in Eq. (12)], the friction coefficient can be described by a function of the variable $S(0)/[S(\mathbf{G}_1)\rho_c]$ for a number of material parameters of the interface, such as fluid and wall densities, surface energy, chain length, and wall lattice type.⁴² The best fit to the MD data taken from Ref. 42 is indicated by the dashed line in Fig. 13. It can be observed that, for all

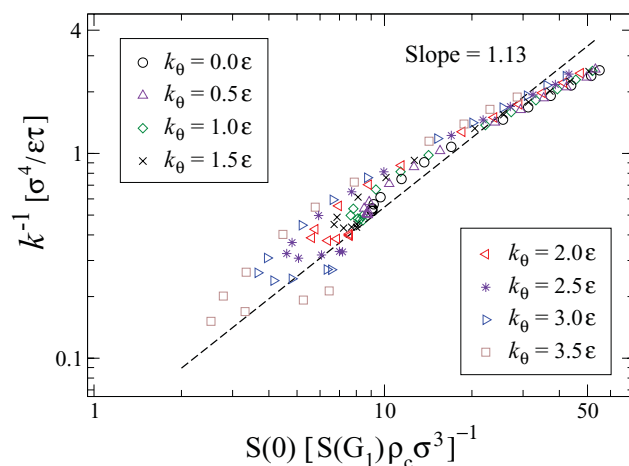


FIG. 13. Log-log plot of the inverse friction coefficient $k^{-1} = V_1/\sigma_{xz}$ (in units of $\sigma^4/\epsilon\tau$) as a function of $S(0)/[S(\mathbf{G}_1)\rho_c\sigma^3]$ computed in the first fluid layer. The values of the bending stiffness coefficient are tabulated in the inset. The dashed line $y = 0.041 x^{1.13}$ is taken from Ref. 42 and it is shown for reference.

values of the bending stiffness coefficient, the data points are distributed around the straight dashed line. In agreement with the previous results,⁴² at small slip velocities, the friction coefficient for more flexible chains, $k_\theta \leq 2.0\epsilon$, is well described by the master curve. The most noticeable difference between flexible and semiflexible chains in Fig. 13 is the appearance of the hook-shaped curvature at small slip velocities, which is related to the local maximum in the structure factor discussed earlier. In other words, the same value of the product of structure factor and contact density, $S(0)/[S(\mathbf{G}_1)\rho_c]$, corresponds to two different values of the friction coefficient, depending on the slip velocity and chain stiffness.

In summary, the results in Fig. 13 for semiflexible chains, $k_\theta \leq 2.0\epsilon$, confirm previous findings that the friction coefficient at small slip velocities is determined by the magnitude of the surface-induced peak in the structure factor and the contact density of the first fluid layer.⁴² The deviation from the master curve for more rigid chains, $k_\theta > 2.0\epsilon$, might be related to the slower relaxation dynamics of the chains in the interfacial region, similar to the trends found in dense polymer films at low shear rates.³⁹ Finally, the collapse of the data for $S(0)/[S(\mathbf{G}_1)\rho_c] \gtrsim 10$ in Fig. 13 might be related to the fact that the friction coefficient is independent of the chain stiffness at large slip velocities (see Fig. 10).

IV. CONCLUSIONS

In this paper, we have presented results from extensive molecular dynamics simulations of thin polymer films confined by crystalline walls with weak surface energy. The computations were based on a coarse-grained bead-spring model of linear polymer chains with an additional bond angle potential that controls chain bending stiffness. The spatial configuration and local relaxation dynamics of polymer chains were characterized by the radius of gyration and the decay rate of the autocorrelation function of the first normal mode. We found that semiflexible chains near solid walls become more uncoiled and their relaxation dynamics is significantly slowed down.

The most interesting result of the present study is the appearance of a distinct maximum in the velocity dependence of the friction coefficient due to the shear-induced alignment of semiflexible chain segments in the first fluid layer near solid walls. At small slip velocities, the orientation of more extended chain segments along the flow direction produces an enhanced ordering within the first fluid layer measured by the height of the main peak in the structure factor. This effect is absent for fully flexible chains since their segment orientation in the adjacent layer remains isotropic at small slip velocities. In addition, it was demonstrated that, with increasing slip velocity, the friction coefficient decreases and becomes independent of the chain stiffness.

Our simulation results indicate that the main features in the shear rate dependence of the slip length include a nearly constant value at low shear rates, a pronounced minimum at intermediate rates, and a rapid increase at high shear rates. These slip flow regimes are determined by the ratio of the shear-rate-dependent polymer viscosity and the dynamic friction coefficient. Overall, we conclude that it is difficult to pre-

dict the net effect of chain stiffness on the slip length without performing numerical simulations; especially at low shear rates, where both polymer viscosity and friction coefficient increase with increasing bending rigidity.

ACKNOWLEDGMENTS

Financial support from the National Science Foundation (CBET-1033662) is gratefully acknowledged. Computational work in support of this research was performed at Michigan State University's High Performance Computing Facility.

- ¹M. M. Denn, *Annu. Rev. Fluid Mech.* **33**, 265 (2001).
- ²E. C. Achilleos, G. Georgiou, and S. G. Hatzikiriakos, *J. Vinyl Addit. Technol.* **8**, 7 (2002).
- ³M. Ruths and J. N. Israelachvili, "Surface forces and nanorheology of molecularly thin films," in *Springer Handbook of Nanotechnology*, 3rd ed., edited by B. Bhushan (Springer, Berlin, 2010).
- ⁴O. Baumchen and K. Jacobs, *J. Phys.: Condens. Matter* **22**, 033102 (2010).
- ⁵S. Q. Wang, *Adv. Polym. Sci.* **138**, 227 (1999).
- ⁶A. Maali and B. Bhushan, *J. Phys.: Condens. Matter* **20**, 315201 (2008).
- ⁷U. Heinbuch and J. Fischer, *Phys. Rev. A* **40**, 1144 (1989).
- ⁸J. Koplik, J. R. Banavar, and J. F. Willemsen, *Phys. Fluids A* **1**, 781 (1989).
- ⁹P. A. Thompson and M. O. Robbins, *Phys. Rev. A* **41**, 6830 (1990).
- ¹⁰P. A. Thompson and S. M. Troian, *Nature (London)* **389**, 360 (1997).
- ¹¹J.-L. Barrat and L. Bocquet, *Phys. Rev. Lett.* **82**, 4671 (1999).
- ¹²J.-L. Barrat and L. Bocquet, *Faraday Discuss.* **112**, 119 (1999).
- ¹³T. M. Galea and P. Attard, *Langmuir* **20**, 3477 (2004).
- ¹⁴N. V. Priezjev, *Phys. Rev. E* **75**, 051605 (2007).
- ¹⁵N. V. Priezjev, *J. Chem. Phys.* **127**, 144708 (2007).
- ¹⁶A. E. Kobryn and A. Kovalenko, *J. Chem. Phys.* **129**, 134701 (2008).
- ¹⁷C. Liu and Z. Li, *Phys. Rev. E* **80**, 036302 (2009).
- ¹⁸X. Yong and L. T. Zhang, *Phys. Rev. E* **82**, 056313 (2010).
- ¹⁹N. Asproulis and D. Drikakis, *Phys. Rev. E* **81**, 061503 (2010).
- ²⁰A. Niavarani and N. V. Priezjev, *Phys. Rev. E* **81**, 011606 (2010).
- ²¹N. Asproulis and D. Drikakis, *Phys. Rev. E* **84**, 031504 (2011).
- ²²A. A. Pahlavan and J. B. Freund, *Phys. Rev. E* **83**, 021602 (2011).
- ²³F.-C. Wang and Y.-P. Zhao, *Soft Matter* **7**, 8628 (2011).
- ²⁴S. K. Kannam, B. D. Todd, J. S. Hansen, and P. J. Daivis, *J. Chem. Phys.* **135**, 144701 (2011).
- ²⁵N. V. Priezjev, *J. Chem. Phys.* **135**, 204704 (2011).
- ²⁶S. K. Kannam, B. D. Todd, J. S. Hansen, and P. J. Daivis, *J. Chem. Phys.* **136**, 024705 (2012).
- ²⁷P. Padilla and S. Toxvaerd, *J. Chem. Phys.* **101**, 1490 (1994).
- ²⁸P. A. Thompson, M. O. Robbins, and G. S. Grest, *Isr. J. Chem.* **35**, 93 (1995).
- ²⁹E. Manias, G. Hadzioannou, and G. ten Brinke, *Langmuir* **12**, 4587 (1996).
- ³⁰R. Khare, J. J. de Pablo, and A. Yethiraj, *Macromolecules* **29**, 7910 (1996).
- ³¹M. J. Stevens, M. Mondello, G. S. Grest, S. T. Cui, H. D. Cochran, and P. T. Cummings, *J. Chem. Phys.* **106**, 7303 (1997).
- ³²A. Koike and M. Yoneya, *J. Phys. Chem. B* **102**, 3669 (1998).
- ³³A. Jabbarzadeh, J. D. Atkinson, and R. I. Tanner, *J. Chem. Phys.* **110**, 2612 (1999).
- ³⁴A. Jabbarzadeh, J. D. Atkinson, and R. I. Tanner, *Tribol. Int.* **35**, 35 (2002).
- ³⁵N. V. Priezjev and S. M. Troian, *Phys. Rev. Lett.* **92**, 018302 (2004).
- ³⁶A. Niavarani and N. V. Priezjev, *Phys. Rev. E* **77**, 041606 (2008).
- ³⁷J. Servantie and M. Muller, *Phys. Rev. Lett.* **101**, 026101 (2008).
- ³⁸A. Martini, H. Y. Hsu, N. A. Patankar, and S. Lichter, *Phys. Rev. Lett.* **100**, 206001 (2008).
- ³⁹N. V. Priezjev, *Phys. Rev. E* **80**, 031608 (2009).
- ⁴⁰S. Dhondt, G. G. Pereira, and S. C. Hendy, *Phys. Rev. E* **80**, 036309 (2009).
- ⁴¹L.-T. Kong, C. Denniston, and M. H. Muser, *Modell. Simul. Mater. Sci. Eng.* **18**, 034004 (2010).
- ⁴²N. V. Priezjev, *Phys. Rev. E* **82**, 051603 (2010).
- ⁴³A. Vadakkepatt, Y. Dong, S. Lichter, and A. Martini, *Phys. Rev. E* **84**, 066311 (2011).
- ⁴⁴M. R. Farrow, A. Chremos, P. J. Camp, S. G. Harris, and R. F. Watts, *Tribol. Lett.* **42**, 325 (2011).

- ⁴⁵D. Savio, N. Fillot, P. Vergne, and M. Zaccheddu, *Tribol. Lett.* **46**, 11 (2012).
- ⁴⁶P. G. de Gennes, *Soft Interfaces, The 1994 Dirac Memorial Lecture* (Cambridge University Press, 1997).
- ⁴⁷W. G. Hoover, D. J. Evans, R. B. Hickman, A. J. C. Ladd, W. T. Ashurst, and B. Moran, *Phys. Rev. A* **22**, 1690 (1980).
- ⁴⁸G. Marechal, J.-P. Ryckaert, and A. Bellemans, *Mol. Phys.* **61**, 33 (1987).
- ⁴⁹J. Servantie and M. Muller, *J. Chem. Phys.* **128**, 014709 (2008).
- ⁵⁰R. B. Bird, C. F. Curtiss, R. C. Armstrong, and O. Hassager, *Dynamics of Polymeric Liquids*, 2nd ed. (Wiley, New York, 1987).
- ⁵¹K. Kremer and G. S. Grest, *J. Chem. Phys.* **92**, 5057 (1990).
- ⁵²R. Auhl, R. Everaers, G. S. Grest, K. Kremer, and S. J. Plimpton, *J. Chem. Phys.* **119**, 12718 (2003).
- ⁵³G. S. Grest and K. Kremer, *Phys. Rev. A* **33**, 3628 (1986).
- ⁵⁴N. V. Priezjev and S. M. Troian, *J. Fluid Mech.* **554**, 25 (2006).
- ⁵⁵N. V. Priezjev, A. A. Darhuber, and S. M. Troian, *Phys. Rev. E* **71**, 041608 (2005).
- ⁵⁶M. P. Allen and D. J. Tildesley, *Computer Simulation of Liquids* (Clarendon, Oxford, 1987).
- ⁵⁷I. Bitsanis and G. Hadziioannou, *J. Chem. Phys.* **92**, 3827 (1990).
- ⁵⁸T. Aoyagi, J. Takimoto, and M. Doi, *J. Chem. Phys.* **115**, 552 (2001).
- ⁵⁹A. Niavarani and N. V. Priezjev, *J. Chem. Phys.* **129**, 144902 (2008).
- ⁶⁰I. A. Bitsanis and C. Pan, *J. Chem. Phys.* **99**, 5520 (1993).
- ⁶¹E. Manias, "Nanorheology of strongly confined molecular fluids," Ph.D. dissertation, (University of Groningen, 1995).
- ⁶²K. Binder, *Monte Carlo and Molecular Dynamics Simulations in Polymer Science* (Oxford University Press, 1995).
- ⁶³M. Bulacua and E. van der Giessen, *J. Chem. Phys.* **123**, 114901 (2005).
- ⁶⁴S. Bernardi, B. D. Todd, and D. J. Searles, *J. Chem. Phys.* **132**, 244706 (2010).